nature synthesis

Article

https://doi.org/10.1038/s44160-024-00657-8

Mechanical exfoliation of non-layered metal oxides into ultrathin flakes

Received: 6 January 2024

Accepted: 5 September 2024

Published online: 3 October 2024

Check for updates

Ruijie Li[1,17], Zhixin Yao[1,2,17], Zhenjiang Li[1,17], Lei Liao[3,17], Huacong Sun[3,17], Chaonan Cong[4,17], Xudan Huang[3], Kang Wu[3], Tingjun Wang[5], Huifeng Tian[1], PeiChi Liao[1], Shizhuo Liu[1], Yihan Wang[1], Lina Yang Zhang[1], U Sasaki[1], Ge Yin[1], Junjie Guo[2], Yu Ye[6], Xiaoding Wei[4,7], Xueyun Wang[5], Jiawang Hong[5], Jinhai Mao[8], Lihong Bao[3,8,9], Lifen Wang[3,9], Xuedong Bai[3,9], Peng Gao[9,10,11], Kaihui Liu[11,12], Lei Liao[13], Jun He[14], Shulin Bai[1], Yanfeng Zhang[1], Yanglong Hou[1], Ruqiang Zou[1], Hong-Jun Gao[3,8,9], Yue Zhang[1,15], Enge Wang[9,10,11,16] & Lei Liu[1,11] ✉

The exfoliation of layered crystals can produce diverse two-dimensional (2D) materials and heterostructures. However, the micromechanical cleavage of non-stratified materials into 2D flakes remains challenging due to *z*-direction consecutive bonding. Here we report a mechanical exfoliation method for producing freestanding 2D metal oxide flakes. By synchronizing the thermal decomposition of metal salts and water-assisted forming, we synthesize large-aspect-ratio lamellae of amorphous and crystalline metal oxides as parent materials, which can exfoliate to ultrathin flakes. The freestanding, transferrable features allow the room temperature integration of high-*k* metal oxide flakes as top-gate dielectrics in 2D material transistors. We utilize the dual-function Cr-doped AlO_x flake as the gating dielectric and component, sensing and storing the visible light by photon-programming floating gate effect, showing an in-sensor computing device. Our results provide a platform to investigate the fundamental properties of ultrathin metal oxides free of substrate clamping and pave the way to metal oxides-based functional devices.

Metal oxides, a class of ceramics formed by metal cations and oxide anions, have comprehensive applications ranging from modern electronics and sensors to energy technology[1–3]. One well-known example is the insulating amorphous metal oxides (AMOs, such as SiO_2 and high dielectric constant (high-*k*) HfO_2), which are critical industrial dielectrics in memory and logic devices[4–6]. Crystalline metal oxides (CMOs) with lattice periodicity are desirable for next-generation electronics devices owing to their versatile physical functionalities such as ferroelectricity and ferromagnetism in three-dimensional (3D) shapes[7]. Recently, by bottom-up growth, freestanding complex oxide thin films have been synthesized and their heterostructures have been obtained via remote epitaxy through graphene or by etching interfacial sacrificial layers[8–11]. On a parallel front, mechanically exfoliating layered crystals to freestanding 2D forms and artificially stacking them by the transfer technique is one method of establishing heterostructures, benefitting from intrinsic periodic interfaces for cleavage[12–17]. The development of a universal method to mechanically exfoliate non-layered materials is of interest but is challenging.

When focusing on metal oxides, a liquid-phase exfoliation starting from the bulk crystals has been successfully applied to six kinds of CMO, which typically undergoes an isotropic exfoliation process, giving rise to limited size particles[18–24]. The touch print approach, which uses the self-limited oxidized layer on metal surfaces, produces seven CMO ultrathin flakes (typically <2 nm)[25–27]. Very recently, the exfoliation of crystalline, intrinsically layered SnO and V_2O_5 to thin flakes has been fulfilled by introducing a transition from a stable to a

A full list of affiliations appears at the end of the paper. ✉e-mail: l_liu@pku.edu.cn

https://doi.org/10.1038/s44160-024-00657-8

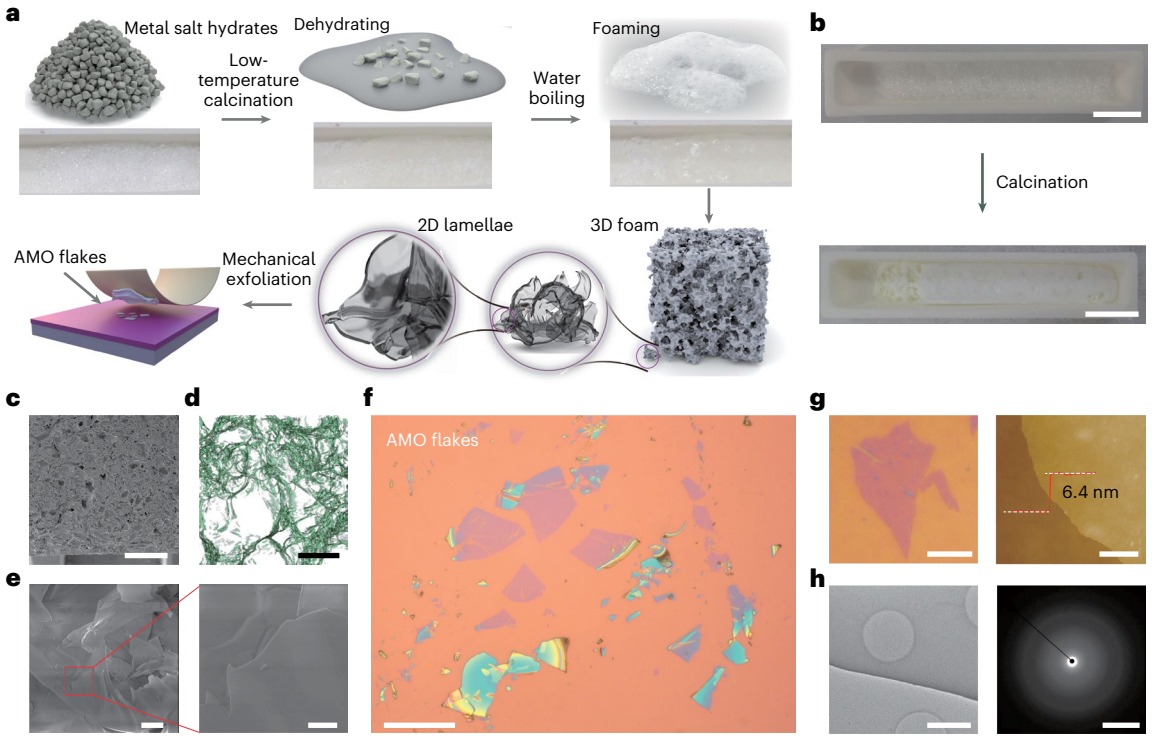

Fig. 1 | Preparation of AMO flakes by the foaming-exfoliation method. **a**, Schematics of the synthesis process. Calcinating metal salt hydrates at low temperatures initiates dehydration and thermal decomposition, enabling the synchronization of the in situ foaming process by water boiling and the growth of AMOs. The obtained 3D AMO foam is composed of holes and thin lamellae of oxides. By the conventional tape exfoliation, the lamellae with large aspect ratios undergo long-range even fracture, producing ultrathin AMO flakes. **b**, Optical images of ANN precursors before and after calcination, displaying the macroscopic porous structures. **c**, SEM image of an AMO foam. **d**, A micro-CT scan of one foam, showing the characteristics of internal porous structures. **e**, SEM characterizations of the foam surface, showing smooth-surfaced lamellae with large aspect ratios (the right panel is an enlarged image of the red box in the left panel). **f**, A representative optical image of exfoliated α-AlO_x flakes. **g**, An AFM image of one ultrathin α-AlO_x flake with a thickness of 6.4 nm. **h**, Low-magnification TEM images and the corresponding SAED result of one exfoliated α-AlO_x flake. Scale bars, 1 mm (**c**), 200 μm (**d**), 20 μm (left panel of **e** and **f**), 5 μm (right panel of **e** and left panel of **g**), 1 μm (right panel of **g**), 500 nm (left panel of **h**) and 5 nm^{-1} (right panel of **h**).

metastable phase[28]. So far, there has been no experimental work (to our knowledge) on the exfoliation of AMOs, probably due to difficulties in obtaining appropriate bulk AMOs materials. Moreover, obtaining uniform thicknesses in AMO and CMO flakes with the capability to tune the thickness, and, more importantly, the novel functionalities beyond high-*k* dielectrics, is of interest.

In this Article, we develop a foaming-exfoliation process as a versatile method to prepare AMO and CMO ultrathin flakes. By coinciding the decomposition of metal salts and water-assisted foaming, large-sized 2D lamellae are obtained that undergo long-range even fracture during tape exfoliation, producing freestanding thin flakes with transferable characteristics. We further show these exfoliated AMO and CMO flakes as one building block that can be incorporated into 2D materials-based heterostructures as high-quality dielectrics and functional components.

Results and discussion

Preparation process of flakes

As sketched in Fig. 1a, the synthesis of ultrathin AMO flakes includes two steps: water-assisted, low-temperature calcination of metal salts to prepare large-sized amorphous (α-) lamellae in a 3D foam and subsequent mechanical exfoliations of AMO lamellae to thin flakes. Here, water serves as a green, efficient foaming agent without any residues left in products. During the thermal decomposition of metal salt hydrates, the water bubbling introduces a large amount of gas release, dramatically altering the morphology of products, giving porous AMO foam containing 2D-like lamellae (up to hundreds of micrometres large but only several micrometres thick) rather than conventional powders in the case of water deficiency. Surprisingly, when using these foams as source materials for the traditional tape exfoliation, ultrathin flakes (5–50 nm thick) with smooth surfaces can be obtained routinely on substrates, bearing a high level of resemblance to the exfoliation of layered crystals but with a very distinct mechanism (see the whole process in Supplementary Video 1). Apart from its simplicity, this foaming-exfoliation methodology allows for the general, rapid synthesis of varied AMO thin flakes with high efficiency.

Taking the precursor aluminium nitrate non-ahydrate (ANN; $Al(NO_3)_3{\cdot}9H_2O$) as an example, calcinating ANN pellets initiates the dehydration (~70 °C) and then successive decompositions are performed that involve amorphous aluminium oxide (α-AlO_x) as intermediate products (<800 °C), ultimately producing crystalline alumina (~1,200 °C); this method has been widely used for decades in the industrial production of alumina powders[29]. In our experiment, when putting several ANN pellets together, the desorption of crystal water molecules accumulated and the conspicuous ebullition, along with the gas release, was observed upon heating (Supplementary Video 2). The thermal decomposition of ANN proceeded simultaneously so that the growth of metal oxides encountered water bubbling, generating cellular foams of α-AlO_x with macroscopic-to-microscopic holes (Fig. 1b, c). Micro-computed tomography (micro-CT) characterization shows internal pores with diameters ranging from tens to hundreds of micrometres (Fig. 1d; see more and detailed analysis in Supplementary Fig. 1 and Supplementary Video 3). Scanning electron microscopy (SEM) images of α-AlO_x foam (Fig. 1e) show oxide lamellae featuring a high degree of surface smoothness and large aspect ratios with a thickness of several micrometres and lateral size of up to hundreds of micrometres

(see cross-section SEM images in Supplementary Fig. 2b,c). X-ray diffraction (XRD) measurements confirmed its amorphous state (Supplementary Fig. 2d).

Surprisingly, by treating these α-foams as starting materials for tape exfoliation (Supplementary Video 1), we can routinely obtain AMO 2D thin flakes (5–50 nm thick) with height-dependent colours and lateral sizes of ~10 μm (Fig. 1f,g, Extended Data Fig. 1, Supplementary Fig. 3 and Supplementary Video 4), very similar to those obtained by exfoliating layered crystals, which have naturally preferential cleavage planes[1–4]. These exfoliated AMO layers hold structural integrity[30] and typically possess flat surfaces and uniform height, by which this exfoliation process is thus referred to as a long-range and even fracture at a 10 μm scale (Extended Data Fig. 2), in sharp contrast to the conchoidal fracture for the bulk of amorphous materials and the faceted fracture for crystals[31,32]. After transferring, selected area electron diffraction (SAED) characterizations of AMO layers confirm the amorphous feature by showing only diffuse halos (Fig. 1h).

To investigate the mechanism of this foaming-exfoliation process for AMO thin flakes, in a control experiment, we found that calcinating a single ANN pellet induced a slight and 'local' water boiling, and the morphology of pellets was kept after calcination (Supplementary Video 5). The final products were submicrometre ultrafine powders, indicating the isotropic growth of AlO_x (Supplementary Fig. 4). Therefore, fierce water boiling and gas release were believed to play a critical role in lamellae structures and foams. While the foaming technique is typically utilized as the post-process preparation of porous polymers and ceramics[33,34], the boiling of desorbed crystal water in this study coincides with the ANN decomposition and the growth of α-AlO_x, resulting in the water-assisted foaming in the growth step and the anisotropic growth towards 2D lamellae. Synchronizing the precursor decomposition (oxide growth) and water boiling (foaming process) is essential, and it only depends on the precursors' physicochemical properties. To corroborate this microscopic mechanism, we investigated more metal nitrate hydrates with decomposition temperatures >100 °C, including Zn and Co (Supplementary Fig. 5a,b), showing only fine particles instead of lamellae after calcination when having water as the forming agent. In sharp contrast, by replacing the forming agent with a high-boiling-temperature solvent, the foaming-exfoliation method works for α-ZnO_x and α-CoO_x (Supplementary Fig. 5c,d). By borrowing the concept of glass-forming ability for amorphous materials, we focus on the glass lamella-forming ability of AMOs in our method. Results in Supplementary Fig. 5 support that the glass lamella-forming ability, as expected, is contingent upon whether precursor decompositions and foaming agent boiling occur concurrently or not.

We further developed the second route toward thin AMO flakes by directly crushing foams on substrates (Supplementary Video 1). Foams broke into smaller and thinner pieces, and thin flakes (thickness <100 nm) can also be obtained at the same locations indicated by pre-fabricated marks on substrates (Extended Data Fig. 3). Although the probability of ultrathin flakes is low, this crushing approach unambiguously verifies the following: (1) thin flakes indeed come from ANN calcines, and (2) thin flakes strongly, if not solely, hinge on the fracture of foams themselves, other than the interaction competition among foam–substrate interfaces and foams inside, signifying a distinct thinning mechanism with that of layered crystalline materials' cleavages. Note that the missing plastic deformation mechanism endows amorphous materials with inherent brittleness[35,36], and AMOs are non-stratified. In our experiment, the third dimensional of the resulting flake lies in the range of sub-ten to tens of nanometres, which has not been experimentally investigated before, to the best of our knowledge. On the other hand, the exfoliation mechanism for the ultrathin AMO layers can be theoretically explained by the mixed-mode cracking behaviour[37]. We use Extended Data Fig. 4 to help visualize the exfoliation mechanism. For lamellae, containing a surface notch on a rigid substrate will introduce fracture in two modes. In mode I, the tensions find the weakest spot on the surface so that a crack initiates and develops vertically, resulting in smaller flakes with the same thickness. In mode II, the bending moment introduces concentrated shear stress on the most severe, probably pre-existing geometrical flaws, initiating a crack that propagates through the longitudinal section and in a perfectly smooth path to produce a thinner flake. Hutchinson and Suo gave the approximation solutions for the mode I and mode II energy release rates as $G_{\mathrm{I}} \sim 3M^2/Eh^3 + \frac{3P^2}{4Eh}$ and $G_{\mathrm{II}} \sim 9M^2/4Eh^3 + \frac{P^2}{Eh}$, respectively, in which M is the bending moment, P is the axial tension, E is Young's modulus and h is the thickness of the delaminated flake[37]. Moreover, to show the mechanical process of the cleavage into thin flakes, we further applied the finite element analysis with the phase field fracture model (Supplementary Figs. 6 and 7)[38]. In short, with the increased pressure, the cracks can steadily propagate horizontally in mode II fashion, which is consistent with the previously theoretical analysis on the delamination of an isotropic elastic solid near a surface flaw (see detailed analysis in Supplementary Note 1 and Supplementary Video 6)[37].

The versatility of the method

To show the method's versatility, we extended the investigations to more AMOs, with Ga from post-transition metals, and Cr, Zr and Hf from transition metals being selected (Fig. 2b). For α-GaO_x, the same water-assisted foaming process, smooth and micrometre-thick lamellae, and ultrathin flakes can be observed with high reproducibility (Supplementary Fig. 8). As for α-CrO_x, yields of lamellae and ultrathin flakes by directly calcinating nitrate nonahydrates were low. Strikingly, adding additional water to dissolve nitrate completely before the calcination can generate adequate foaming and enlarge lateral sizes of α-lamellae, enormously improving the chance of α-CrO_x thin flakes by exfoliations (Supplementary Fig. 9). With the strategy of artificially adding extra water as forming agents, we further applied this method to more AMOs in which originally there was no water boiling by heating hydrate precursors only. For example, only fine powders of α-ZrO_x were prepared by calcinating zirconium nitrate pentahydrate (Supplementary Fig. 10). By heating the aqueous solution, the overall geometry changed dramatically; lamellae (>100 μm) and thin flakes were successfully fabricated by the exfoliation (Supplementary Fig. 10). Moreover, if the metal nitrates were commercially unavailable or costly, this foaming-exfoliation method would still work with other salt precursors. We used hafnium dichloride oxide octahydrate as the precursor for preparing α-HfO_x flakes (Supplementary Fig. 11). Furthermore, by introducing a high-boiling-point solvent (for example, ethylene glycol) to synchronize the foaming and decomposition, α-InO_x and α-MoO_x thin flakes were able to be obtained by the exfoliation (Fig. 2b). The glass lamella-forming abilities of mono-AMOs we have explored are summarized and visually represented in Fig. 2a (Supplementary Fig. 12). Also, the water-assisted foaming process guarantees the atomic-level mixing of multiple metal ions in the aqueous solution before calcination, allowing us to prepare complex bi- and polymetallic oxide flakes. We demonstrated the synthesis of ternary ZrAlO and quaternary AlHfZrO flakes by simply mixing precursors (Fig. 2b, Supplementary Figs. 13 and 14, and Supplementary Note 2). All of the detailed synthesis conditions of metal oxides are listed in Supplementary Table 1.

Another aspect to discuss is the yield and thickness control of AMO thin flakes. As exemplified by α-AlO_x, we show the statistical analysis on the counts of large flakes in Extended Data Fig. 1. Typically, one can find tens of thin flakes on one SiO_2/Si substrate, similar to the yield of 2D materials by the tape exfoliation. Another example of the high yield of exfoliated thin flakes is displayed in Supplementary Fig. 15 for α-ZrO_x. A series of mechanical exfoliations of all of the metal oxides investigated here have been conducted (Supplementary Figs. 16 and 17); the yield, which is defined by the number of thin flakes over the area, has been calculated and presented in Supplementary Table 2. Moreover, the heating rate has been revealed as an effective parameter to tune yields

https://doi.org/10.1038/s44160-024-00657-8

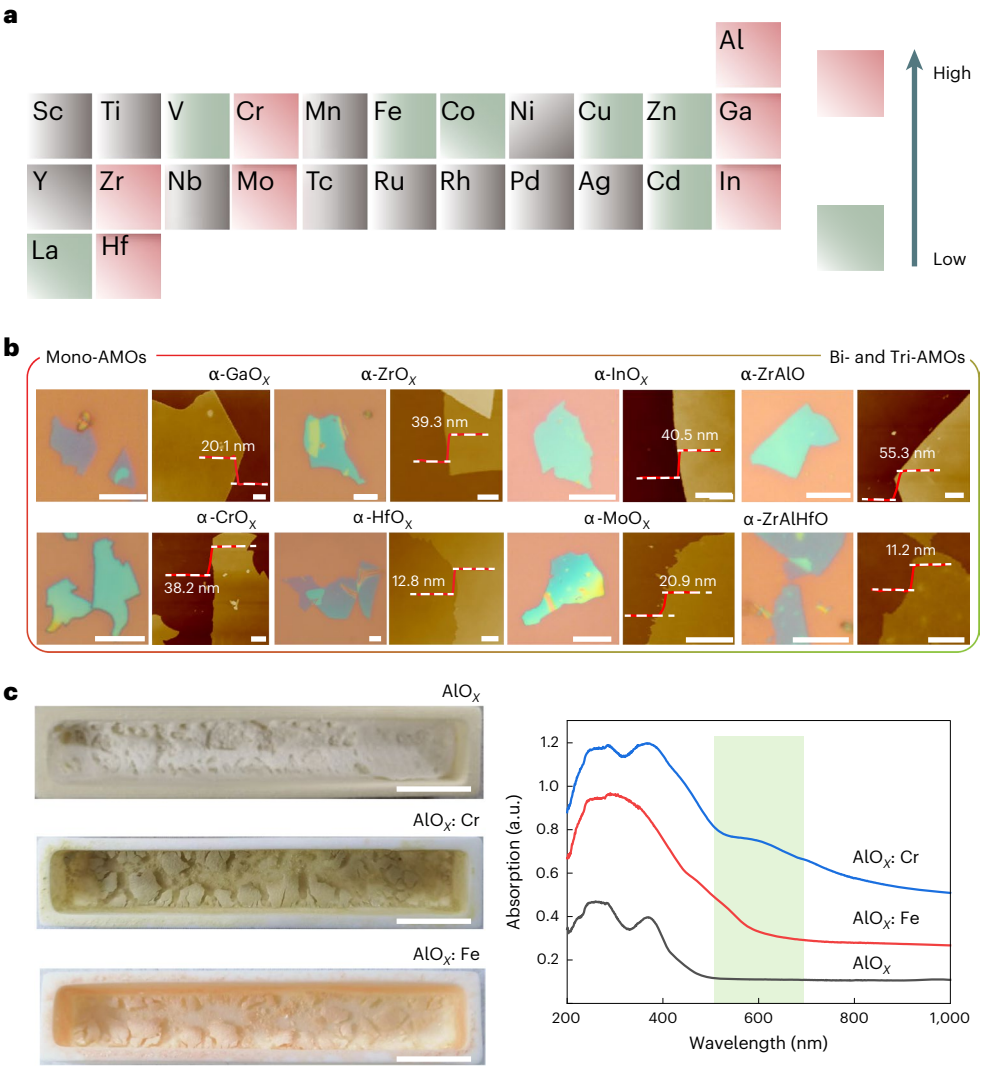

Fig. 2 | A library of foaming-exfoliation-derived AMO flakes. a, Overview of AMOs with high (pink) and low (green) glass lamella-forming abilities. **b**, Representative optical images and AFM characterizations (thickness determined by the white lines) of exfoliated mono-, bi- and tri-AMO flakes. **c**, Optical images (left) and absorption spectra (right) of pristine, Cr-doped and Fe-doped α-AlO$_x$ samples, respectively, showing enhanced absorption in the range of 500–700 nm by doping. Scale bars, 10 μm (optical images in **b**) and 1 μm (AFM images in **b**).

for certain metal oxides (Supplementary Figs. 18–21, Supplementary Note 3 and Supplementary Table 3). Furthermore, liquid exfoliation has proven effective for metal oxide flakes (Supplementary Figs. 22–24 and Supplementary Note 4). At this moment, it is hard to control the thickness of one specific AMO flake using this method. However, for application, one can always pick up the flakes with desired thicknesses, for example, 20–40-nm-thick high-*k* AMO flakes for top dielectrics with acceptable leakage currents.

Here, we emphasize the capability of doping in AMOs, which gives rise to novel metal oxide flakes that possess unique properties and functionality that can be incorporated into devices. For example, we show the doping of amorphous AlO$_x$ by Cr (CrAlO) or Fe (FeAlO), in analogy with the sapphire and ruby (Cr- and Fe-doped crystalline Al_2O_3, respectively). The colour of calcines changed dramatically, accompanied by increased optical absorption in the range of 500–700 nm (Fig. 2c). Note that the freestanding amorphous CrAlO thin flakes were not prepared by other methods before and investigated in devices. Thereby, the doped AMOs with multitudinous choices on matrixes and dopants can provide a new type of nanomaterials with tunable physical properties.

By increasing calcination temperatures (T_{cal}) to improve crystallinities, we further demonstrate the preparation of CMO thin flakes by this foaming-exfoliation process (Supplementary Table 4). As shown in Fig. 3a,b, apart from the 7 metal oxides with high glass lamella-forming abilities (Fig. 2a), we extended the library of foaming-exfoliation-derived CMO flakes to 6 more metal oxides (total of 13 CMOs) with isolated flakes with flat surfaces (Supplementary Figs. 25 and 26). SAED results show multiple sets of diffraction spots with twisted angles suggesting a polycrystalline feature (Fig. 3b and Supplementary Fig. 27). High-resolution transmission electron microscope (TEM) images show that the crystal size can be controlled by T_{cal}. When T_{cal} is relatively low (but above the crystallization temperature points), the sub-10 nm crystallites with varied orientations are interfaced with amorphous regions (Supplementary Fig. 27). Moreover, increasing T_{cal} leads to the increase of crystallinities manifested by the larger, well-defined nanocrystallites with recognizable grain boundaries and the absence of vitreous regions (Supplementary Fig. 28).

The lattice periodicity in CMOs endows versatile physical functionalities, such as ferromagnetism and ferroelectricity. Accordingly, we examined whether or not the exfoliated, crystalline (Hf, Zr)O_2 (*c*-HfZrO) flakes possessed ferroelectricity by piezoresponse force microscopy (PFM). As displayed in Fig. 3e, hysteresis loops of phase and amplitude curves of four cycles were taken randomly on one exfoliated HfZrO

https://doi.org/10.1038/s44160-024-00657-8

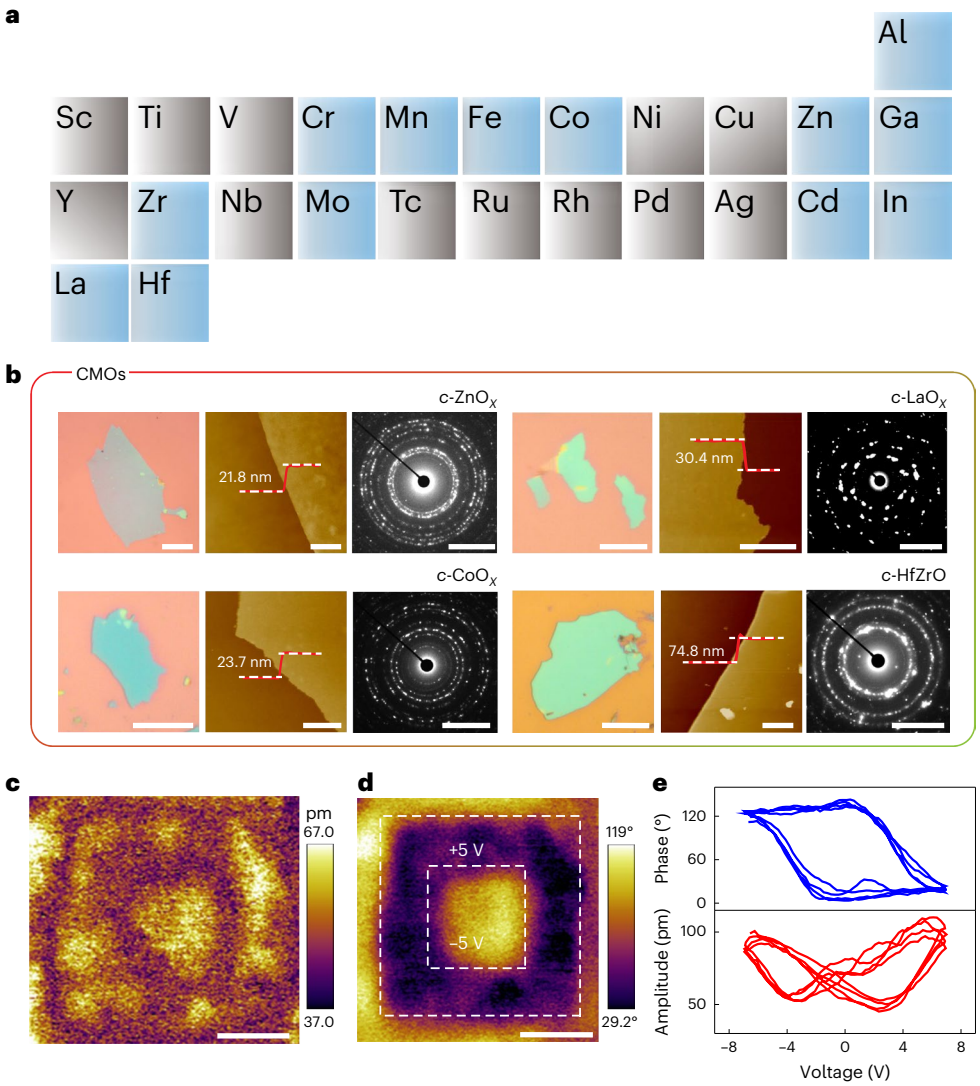

Fig. 3 | The library of as-derived CMO flakes. a, Overview of 13 CMOs (blue box) prepared by the foaming-exfoliation process. **b**, Optical images, AFM (thickness determined by the white lines) and electron diffraction characterizations of four representative CMO flakes. **c**,**d**, Amplitude (**c**) and phase images (**d**) of the HfZrO flake after a box-in-box (dashed boxes) domain switching experiment. The initial polarization direction is downwards, corresponding to the yellow domain. **e**, Phase and amplitude hysteresis by PFM measurements. Scale bars, 5 µm (optical images in **b**), 1 µm (AFM images in **b**–**d**) and 5 nm^{-1} (SAED in **b**).

flake, exhibiting a coercive field of 1.19 MV cm^{-1} (refs. 39–41). The robust ferroelectricity of exfoliated HfZrO flakes is further supported with the domain switching by applying a box-in-box (+5 V outside and −5 V inside), which is stable after 24 h (Fig. 3c,d), confirming the functionality preservation in the exfoliated CMO flake.

Applications of exfoliated flakes

With the polymer-assisted transfer technique initially developed for 2D layered crystals, AMO and CMO flakes can also be transferred onto the target 2D materials to achieve the van der Waals integration, forming vertical 3D–2D heterostructures. Atomic force microscope (AFM) characterizations showed no overt contaminations, height changes or wrinkles on the α-AlO$_x$ flake after the assembly (Fig. 4a and Supplementary Fig. 29). Dual-gated 2D materials field-effect transistors (FETs) are thus feasible by transferring AMO or CMO flakes as top-gate dielectrics (Fig. 4b, Supplementary Figs. 30 and 31 and Supplementary Note 5). Interestingly, a ~1-nm wide gap between the MoS_2 channel and top AMO dielectric was revealed by the cross-section scanning TEM (STEM) characterizations (Fig. 4c, Supplementary Figs. 32 and 33 and Supplementary Note 6), consistent with nanogaps that existed in 2D semiconductor FETs with transferred top dielectrics[18,19,42]. This nanometre gap excludes the damages or doping to the semiconductor in principle when compared with the conventional atomic layer deposition process in which a considerable n-doping effect on MoS_2 occurs, and the interface impurities adversely affect the device performance (the subthreshold swing (SS) and hysteresis)[43,44]. Moreover, the separation of dielectric preparation and device integration in our method allows high preparation temperature for dielectrics, for example, crystalline ZrO_2 (*c*-ZrO_2) synthesized at 450 °C, ensuring the high quality of insulators and suppressing current leakage.

Figure 4d,e shows the output (V_{ds}–I_{ds}) and transfer (V_{tg}–I_{ds}) characteristics of a monolayer MoS_2 gated by one transferred *c*-ZrO_2 flake (ds, drain source; tg, top gate). A current on/off ratio (I_{on}/I_{off}) of over 1×10^8 at $V_{ds} = 0.4$ V is observed. For a wide range of V_{ds} (0.1–0.5 V), SS values as small as 70 mV dec^{-1} and hysteresis width of 2.7 mV (MV cm^{-1})$^{-1}$ (Fig. 4g) are found, both of which are among the best values for monolayer MoS_2 FETs (Supplementary Tables 5 and 6), indicating an ultralow interfacial trap density ($D_{it} \approx 7.6 \times 10^{11}$ cm^{-2} eV^{-1}) and low near-interfacial border trap, both of which benefit from the nanogapped dielectric contact and high-quality insulators[13]. Note that for 2D material FETs, the van der Waals integration of electrodes onto channels has been widely investigated[45]; the nanogapped contact between various

https://doi.org/10.1038/s44160-024-00657-8

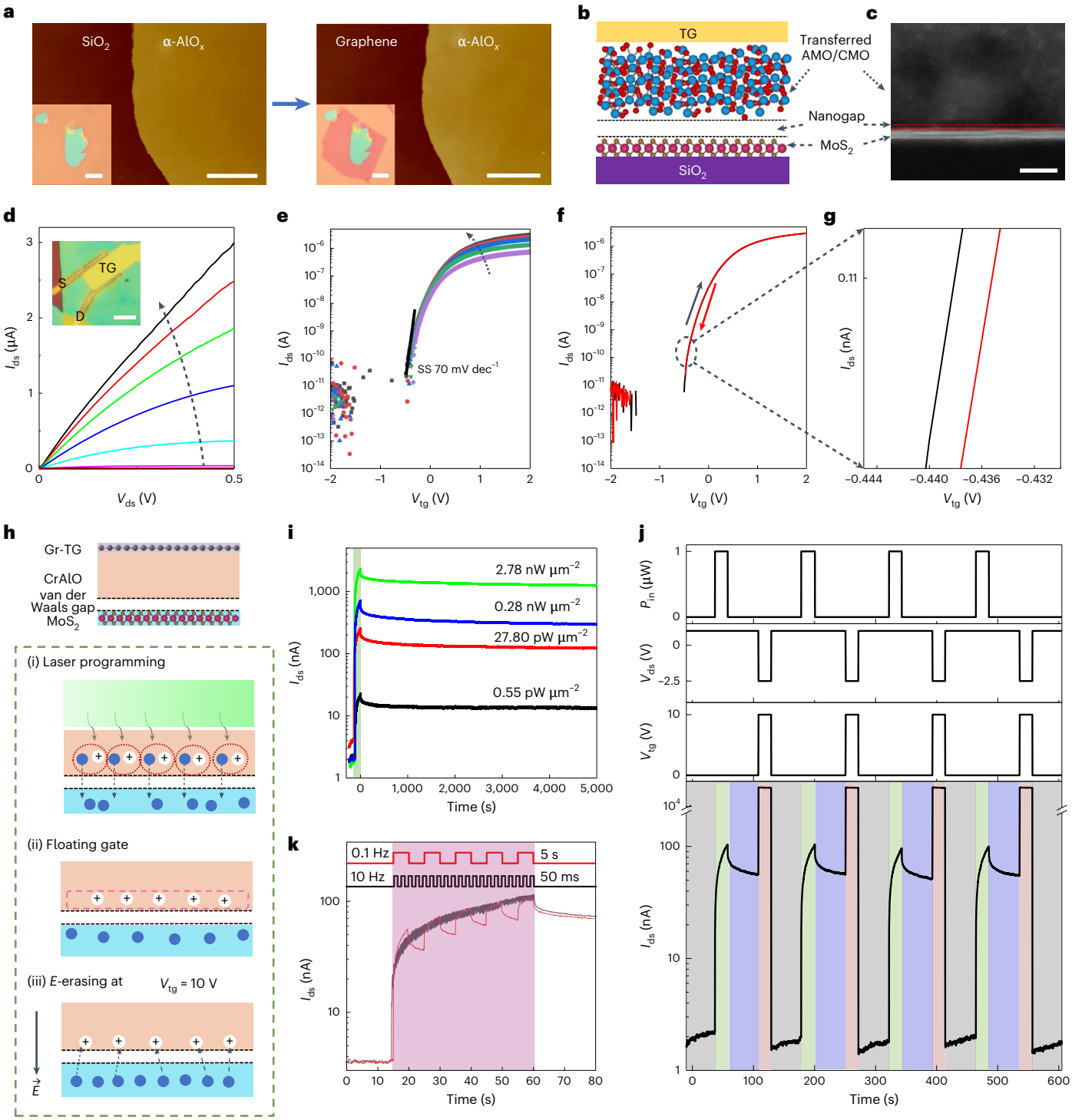

Fig. 4 | Van der Waals integration of exfoliated AMO/CMO flakes and electronic applications. a, AFM and optical (inset) characterizations of one α-AlO_x transferring onto a graphene flake. **b**,**c**, Schematic with blue atoms indicating metal and red atoms indicating oxygen (**b**) and a cross-section STEM image of a 3D–2D heterostructure (**c**), showing a ~2-nm-wide gap between one monolayer MoS_2 and transferred metal oxide flake. TG, top gate. **d**,**e**, V_{ds}–I_{ds} (**d**), where V_{tg} is −2 to 2 V with a step of 0.4 V (the V_{tg} gradually increases along the dotted arrow, and the black line is up to 2 V), and V_{tg}–I_{ds} characteristics (**e**), where V_{ds} is 0.1–0.5 V (the purple line to the black line, that is, along the dotted arrow) with a step of 0.1 V, of a dual-gate monolayer MoS_2 FET with one *c*-ZrO_x flake as the top dielectric, showing the SS of 70 mV dec^{-1}. The inset in **d** shows the optical image of the as-fabricated FET. S, source; D, drain. **f**,**g**, Double-sweep transfer curve of the *c*-ZrO_x-gated MoS_2 device, showing an ultrasmall hysteresis width of 2.7 mV (MV cm^{-1})$^{-1}$. **g** is the enlarged image of the black circle in **f**. The black curves indicate the forward scan (balck arrow), and the red curves indicate the reverse scan (red arrow). **h**,**k**, A photon-programming floating gating device is shown. The device structure and three operations, including the laser programming (i), floating gate after turning the light off (ii) and erasing by a positive gate voltage (iii), are shown (**h**), and by applying optical spikes, the long-term plasticity is revealed in the photon-programming floating gating optoelectronic device (**k**). **i**, The retained channel current is programmed by the laser power densities (different color lines represent different power densities). **j**, Four sensing memory-erasing cycles are shown. Scale bars, 10 μm (insets of **a**), 5 μm (inset of **d**), 500 nm (**a**) and 5 nm (**c**).

high-*k* dielectrics (or other functions) and semi-conductors is the indispensable supplement towards full-gapped contact devices with high performance[6,18,19,42]. More in-depth investigations of using transferred oxide flakes as dielectrics have been performed (Supplementary Figs. 34–37 and Supplementary Note 7)[46–50].

Apart from the dry integration, the deep engineering of metal oxides allows unprecedented properties and functions, for example, the considerable response to the green light irradiation for Cr-doped AlO_x (CrAlO; Fig. 2c). Here, we demonstrate that in one FET the dual-functional CrAlO insulator works as the gating dielectric and component sensing and storing visible light information in a non-volatile way by the photon-programming floating gate, followed by the in-memory process. We first investigated the dielectric function of the transferred CrAlO flake in a top-gated MoS_2 FET (Supplementary Fig. 38), which exhibits an I_{on}/I_{off} of ~1×10^6, negligible leakage current and small hysteresis of 18.5 mV (MV $cm^{-1})^{-1}$. As shown in Fig. 4i, when applying a green light stimulus, the channel current increases by two to three orders of magnitude. In sharp contrast to a conventional photocurrent, which decays severely and promptly after removing the stimulus, a non-volatile optoelectronic memory function is revealed by a stored, retained channel current after turning the light off. We further show the ability to set the retained current over two orders of magnitude by programming incident powers (P_{in}) and the stability in a 5,000 s time frame. In a MoS_2 FET top gated by an undoped AlO_x flake, after the stimulus, the channel current drops quickly with a volatile response (Extended Data Fig. 5b), bearing a high level of resemblance to conventional photocurrents.

Different from the floating gate non-volatile memory[51,52], a photon-programming floating gate effect that senses and stores the light information is proposed and sketched in Fig. 4h (see more details in Extended Data Fig. 5a). Due to the enhanced green light absorption of dielectrics by doping, electron–hole pairs are generated upon the illumination and dissociated, followed by electron tunnelling to MoS_2 through the nanogap. With the light off, the near-interfacial holes cannot be recombined by, for example, electrons in MoS_2, due to the nano-sized gap, and therefore can serve as the robust floating gate responsible for the retained channel current in Fig. 4i. The pure light programming in such devices denies the necessity of any gate voltage involved (V_{tg} = 0 V). We found the extremely low memory threshold power of light (0.55 pW μm^{-2}) in our photon-programming floating gating devices. Note that both key points of the photon-programming floating gating effect, dielectrics with a response to visible light and nanogap to preserve the stored charges, stem from our foaming-exfoliation transfer method.

Holes of the floating gate can be electrically erased by applying V_{tg} of 10 V, which facilitates the electron injection from MoS_2 to CrAlO and the consequent neutralization of trapped holes at the interfaces. The electrical erasing process had a strong anti-jamming capability, that is, when the applied positive V_{tg} for erasing is 10 V, only one-way electron tunnelling (from MoS_2 to CrAlO) is allowed, which ensures the erasing operation even simultaneously under the illumination and leads to one propositional logic operation, the negation of an implication ($\neg(p \rightarrow q)$) ;Extended Data Fig. 5g). As shown in Fig. 4j, the light programming and electrical erasing in photon-programming floating gating devices are highly repeatable. Moreover, we demonstrated in-sensor Boolean logic operations, *p* and *p* AND *q*, in a photon-programming floating gating device (Supplementary Fig. 39). Furthermore, the photon-programming floating gating optoelectronic device has the potential as a synaptic device for in-memory neuromorphic computing and the long-term plasticity modulated by optical spikes is displayed in Fig. 4k.

Here, we note that, although previously some types of CMO have been shown to be thinned down by liquid exfoliation or touch print[7,8,21–28], to the best of our knowledge, there are very few examples of the use of these exfoliated AMO and CMO flakes in 2D materials-based electronic devices (only very recently, crystalline strontium titanium oxide as high-*k* dielectrics)[18,19], not to mention the functionality induced by the oxide components. The dual-functional CrAlO flakes introduced here as one example demonstrate that our method can bring new opportunities for 2D heterostructures by merging the functions of ceramics into the conventional vdW devices. Moreover, with the advent of 2D amorphous materials[53–56], the freestanding, ultrathin AMO flakes, as an indispensable prototype, offer the platform to explore the fundamental amorphous physics in 2D space[57,58].

Conclusions

We report a foaming-exfoliation method to prepare AMO and CMO thin flakes. The atomic-level premixing of precursors in solutions guarantees the synthesis of polymetallic oxides and controlled doping. The ultrathin, transferrable and freestanding features of oxide flakes can be integrated with 2D materials, giving dual-function dielectrics in 2D electronics and photon-programming floating gating heterostructures. The naturally non-existent shapes, including 3D continuous foam, high-aspect-ratio lamellae and 2D thin flakes, of AMOs and CMOs may also be used in other fields such as catalysis and batteries.

Methods

Synthesis of AMO and CMO foams

The commercial metal salts utilized as precursors in our experiments are as follows: $Al(NO_3)_3{\cdot}9H_2O$ (three types: ≥98% from Sigma-Aldrich; 99.99% metal basis from Macklin; 98.0–102.0% from Alfa Aesar), $Ga(NO_3)_3{\cdot}H_2O$ (99.99%), $Cr(NO_3)_3{\cdot}9H_2O$ (99.95% metals basis), $Zr(NO_3)_4{\cdot}5H_2O$ (99.9% trace metals basis), $Cl_2HfO{\cdot}8H_2O$ (98% trace metals basis excluding Zr), $In(NO_3)_3{\cdot}4H_2O$ (99.9%), $(NH_4)_6Mo_7O_{24}{\cdot}4H_2O$ (99%), $Co(NO_3)_2{\cdot}6H_2O$ (99.99%), $La(NO_3)_3{\cdot}6H_2O$ (99.99%), $Cd(NO_3)_2{\cdot}4H_2O$ (99.9%), $Fe(NO_3)_3{\cdot}9H_2O$ (99%), $Zn(NO_3)_2{\cdot}6H_2O$ (99%), and $Mn(NO_3)_2{\cdot}4H_2O$ (98%). All of the metal oxide foams were prepared with a similar calcination process. As exemplified by α-AlO_x, a crucible with 5 g of ANN was put in a Muffle furnace, followed by the calcination at 800 °C for 2 h ramped at a rate of 13 °C min^{-1} in an air atmosphere and then slowly cooling down to room temperature. For experiments of adding extra water, deionized (DI) water was introduced into a crucible containing the metal precursor with gentle stirring, ensuring complete dissolution. Different T_{cal} was also tried if needed. We note that it is necessary to apply extra water to ANN from Alfa Aesar to obtain foams, probably due to the insufficient content of crystal water. The T_{cal} was 510 °C for α-GaO_x and 250 °C for α-CrO_x, respectively. Amorphous ZrO_x foams (T_{cal}: 250 °C) can only be produced by adding more DI water, since directly heating $Zr(NO_3)_4{\cdot}5H_2O$ powders cannot initiate bubbling. The precursor for amorphous HfO_x foams was $Cl_2HfO{\cdot}8H_2O$ with 250 °C of T_{cal}. Amorphous InO_x foams (T_{cal}: 250 °C) can be produced by adding DI water and ethylene glycol (EG). For amorphous MoO_x foams, T_{cal} of 350 °C was selected with EG as the foaming agent. The polymetallic oxide foams were prepared by a similar process with dissolving corresponding metal salts at designed ratios. The optimized T_{cal} was 350 °C and 250 °C, respectively, for ZrAlO and ZrAlHfO. The furnace calcination under 20 cm^{-3} min^{-1} of NH_3 was utilized for ZrAlO, by which the probability of ultrathin flakes was increased.

CMO foams were produced by the calcination at elevated temperatures. The T_{cal} was 1,100 °C for *c*-AlO_x, 600 °C for *c*-GaO_x, 700 °C for *c*-CrO_x (introducing 40 cm^{-3} min^{-1} of NH_3), 450 °C for *c*-ZrO_x (introducing 40 cm^{-3} min^{-1} of NH_3), 500 °C for *c*-HfO_x, 350 °C for *c*-ZnO_x (adding EG), 230 °C for *c*-CoO_x, 250 °C for *c*-MnO_x, 550 °C for *c*-MoO_x, 730 °C for *c*-LaO_x, 450 °C for *c*-CdO_x, and 310 °C for *c*-InO_x and *c*-FeO_x (adding EG and DI water), respectively.

Exfoliation of AMO and CMO thin flakes

The 4 cm-by-1 cm SiO_2/Si chip was first cleaned by the sonication in acetone and then isopropyl alcohol, followed by a nitrogen gas blow. It was further treated with medium-power oxygen plasma for 2 min. The first route (route 1) of the mechanical exfoliation is assisted by

the Scotch magic tape as shown in Supplementary Video 1. Typically, ~0.1 g of AMO/CMO foams was put on the tape with the subsequent folding–unfolding process three to four times; then, the tape was put on the pre-cleaned Si chip with very gentle pressing. After peeling off the tape, the Si chip was investigated by the optical microscope to identify thin AMO/CMO layers. In route 2, the AMO/CMO foam was directly put onto the pre-cleaned Si chips, followed by mechanical crushing with tweeze tips.

Transfer process

Thin layers of exfoliated AMOs/CMOs on SiO_2/Si substrates were transferred onto the TEM grid with the assistance of polycarbonate (PC; 10 wt.% in chloroform) film. The PC solution was spin-coated on the chip. After 1–2 min baking at 110 °C, this PC film was manually peeled from the Si chip and put onto the Quantifoil TEM grids (Au, 300 mesh). With a post-baking (10 min at 150 °C), the PC film was softened and attached well with grids. Then, PC films were removed by several runs of acetone and hot chloroform baths. To transfer the AMO flakes as top dielectrics, a transparent elastomer stamp, polydimethyl siloxane (PDMS), was cut into a 1 cm by 1 cm piece. The PC film with exfoliated flakes was put onto PDMS with short-time baking. The whole stack was then transferred onto a homemade aligned transfer stage with heating capability. The flakes were identified under an optical microscope and manually aligned to the target layers (graphene, MoS_2 or black phosphorus (BP) in the glovebox). The stage temperature was set to be ~100 °C. After several minutes, the PDMS was peeled off slowly. The top PC film was then removed by chloroform vapour for 1–2 h. For PFM measurements, exfoliated HfZrO flakes were transferred onto the Au-coated SiO_2 /Si substrate.

Sample characterizations

The micro-CT characterizations for the porous foams were done by SKYSCAN 1272, Bruker Corporation. SEM imaging was performed by using TESCAN VEGA 3 LMH with tungsten-heated cathodes. The X-ray photoelectron spectroscopy (XPS) spectroscopy measurements were conducted using the Axis Supra. XRD data were acquired by a SmartLab 9KW with Cu Kα radiation. The diffuse reflectance absorption spectra of AMOs were obtained by the Agilent Cary 7000 equipped with an integrating sphere with a barium sulfate coating. For the thickness measurement of exfoliated flakes, AFM measurements were done by Dimension Icon, Bruker Corporation. Energy dispersive spectrometer (EDS) and EDS mapping were obtained by HITACHI S-4800. TEM and electron energy loss spectroscopy (EELS) characterizations have been conducted in a double spherical corrected ARM-300 at a low acceleration voltage (80 kV) with an electron-counting K2 camera. Brunauer–Emmett–Teller data were acquired by ASAP 2020.

PFM

PFM measurements were performed using an atomic force microscope (Asylum Research MFP-3D) with Pt/Ir-coated Si cantilever tips (PPP-EFM-50). The PFM images were taken in the presence of an alternating current voltage (1 V) and a drive frequency of ~350 kHz. Domain switching was realized by applying an electric bias to the AFM probe. Hysteresis loops were measured by dual alternating current resonance tracking PFM mode.

FEA and phase field fracture model

Finite element analysis (FEA) with the phase field fracture model was carried out to simulate the process of AMOs cleaving into nano-sheets. The field phase model employs a continuous scalar phase field d (ranging from 0 to 1) to regularize cracks, with $d = 0$ representing the intact state and $d = 1$ indicating the complete fracture state. We adopted the linear elastic fracture phase field model, which used the quadratic crack geometric function and degradation function. The phase field model was implemented in the commercial FEA software ABAQUS through the user-defined material subroutine (UMAT).

Device fabrication and measurement

To fabricate the devices for electric breakdown characterizations, the AMO flakes were first prepared on one SiO_2/Si substrate. The bottom electrodes with typical widths of 10 μm were patterned by standard electron beam lithography (Tescan VEGA 3) on another Si substrate with a 285-nm-thick oxide, followed by the metal deposition (20 nm of Au) and conventional lift-off process. The target flakes were transferred onto the bottom electrodes, followed by AFM measurements. The top electrodes (70 nm of Au) were fabricated with the same procedures as the bottom ones. For the dual-gate FETs, graphene and MoS_2 monolayers were mechanically exfoliated by the thermally assisted transfer technique and first identified by the optical microscope. Raman and photoluminescence (PL) (for MoS_2 only) measurements were applied to ensure their monolayer characteristics. Source and drain electrodes (10 nm of In/40 nm of Au) were fabricated by standard electron beam lithography (EBL) and metal deposition with top high-k thin flakes of AMOs/CMOs transferred. Au 70 nm thick was used as the top-gate electrode. For the fabrication of BP FETs, the exfoliation of BP and assembly of α-AlO_x were conducted in the glovebox. To fabricate FETs with etched graphite as contacted, graphite was patterned and then etched. Few-layered BP flakes were transferred on electrodes with PDMS, and then high-k thin flakes of AMOs/CMOs were transferred and aligned onto the channel materials of FETs, followed by the deposition of top-gate electrodes. Cr/Au (3 nm/25 nm) were used as source/drain electrodes, and Cr/Au (6 nm/90 nm) were used as top-gate electrodes. Before the electric measurements, all the devices were thermally annealed at 190 °C under 500 cm^{-3} min^{-1} of Ar for 1 h. The electric breakdown measurements were carried out in a probe station (ZEPTOOLS, LNP50-4) at room temperature under vacuum with a Keithley 2614B SourceMeter. Electrical measurements of dual-gated graphene and MoS_2 FETs were carried out in a vacuum probe station (~3×10^{-6} Torr) at room temperature by a Keithley 2614B and 2401 SourceMeter. For BP FETs, transport measurements were performed in a Janis cryostat (~1×10^{-6} mbar) with a helium compressor and lakeshore 331 temperature controller. Electrical data were recorded by a Keithley 4200 SCS system.

Data availability

All data that support the findings of this study are available in the Article and Supplementary Information. Source data are provided with this paper.

References

1. Védrine, J. C. (Ed.). *Metal Oxides in Heterogeneous Catalysis* (Elsevier, 2018).
2. Yu, X., Marks, T. J. & Facchetti, A. Metal oxides for optoelectronic applications. *Nat. Mater.* **15**, 383–396 (2016).
3. Wu, Y. (Ed.). *Metal Oxides in Energy Technologies* (Elsevier, 2018).
4. Illarionov, Y. Y. et al. Insulators for 2D nanoelectronics: the gap to bridge. *Nat. Commun.* **11**, 3385 (2020).
5. Hosono, H. Ionic amorphous oxide semiconductors: material design, carrier transport, and device application. *J. Non. Cryst. Solids* **352**, 851–858 (2006).
6. Wang, Z. et al. Memristors with diffusive dynamics as synaptic emulators for neuromorphic computing. *Nat. Mater.* **16**, 101–108 (2017).
7. Spaldin, N. A. & Ramesh, R. Advances in magnetoelectric multfirroics. *Nat. Mater.* **18**, 203–212 (2019).
8. Lu, D. et al. Synthesis of freestanding single-crystal perovskite films and heterostructures by etching of sacrificial water-soluble layers. *Nat. Mater.* **15**, 1255–1260 (2016).
9. Kum, H. S. et al. Heterogeneous integration of single-crystalline complex-oxide membranes. *Nature* **578**, 75–81 (2020).
10. Huang, J.-K. et al. High-k perovskite membrances as insulators for two-dimensional transistors. *Nature* **605**, 262–267 (2022).

11. Yang, A. J. et al. Van der Waals integration of high-*k* perovskite oxides and two-dimensional semiconductors. *Nat. Electron.* **5**, 233–240 (2022).
12. Novoselov, K. S. et al. Electric field effect in atomically thin carbon films. *Science* **306**, 666–669 (2004).
13. Novoselov, K. S. et al. Two-dimensional atomic crystals. *Proc. Natl Acad. Sci. USA* **102**, 10451–10453 (2005).
14. Liu, F. et al. Disassembling 2D van der Waals crystals into macroscopic monolayers and reassembling into artificial lattices. *Science* **367**, 903–906 (2020).
15. Huang, Y. et al. Universal mechanical exfoliation of large-area 2D crystals. *Nat. Commun.* **11**, 2453 (2020).
16. Geim, A. K. & Grigorieva, I. V. Van der Waals heterostructures. *Nature* **499**, 419–425 (2013).
17. Liu, Y., Huang, Y. & Duan, X. F. Van der Waals integration before and beyond two-dimensional materials. *Nature* **567**, 323–333 (2019).
18. Kaur, H. & Coleman, J. N. Liquid-phase exfoliation of nonlayered non-van-der-Waals crystals into nanoplatelets. *Adv. Mater.* **34**, 2202164 (2022).
19. Balan, A. P. et al. Exfoliation of a non-van der Waals material from iron ore hematite. *Nat. Nanotechnol.* **13**, 602–609 (2018).
20. Balan, A. P. et al. A non-van der Waals two-dimensional material from natural titanium mineral ore ilmenite. *Chem. Mater.* **30**, 5923–5931 (2018).
21. Yadav, T. P. et al. Chromiteen: a new 2D oxide magnetic material from natural ore. *Adv. Mater. Interfaces* **5**, 1800549 (2018).
22. Guan, G. et al. Electrostatic-driven exfoliation and hybridization of 2D nanomaterials. *Adv. Mater.* **29**, 1700326 (2017).
23. Tai, Z. et al. Few atomic layered lithium cathode materials to achieve ultrahigh rate capability in lithium-ion batteries. *Adv. Mater.* **29**, 1700605 (2017).
24. Liu, S. et al. Facile preparation of novel and active 2D nanosheets from non-layered and traditionally non-exfoliable earth-abundant materials. *J. Mater. Chem. A* **7**, 15411–15419 (2019).
25. Zavabeti, A. et al. A liquid metal reaction environment for the room-temperature synthesis of atomically thin metal oxides. *Science* **358**, 332–335 (2017).
26. Zhang, B. Y. et al. Hexagonal metal oxide monolayers derived from the metal–gas interface. *Nat. Mater.* **20**, 1073–1078 (2021).
27. Zavabeti, A. et al. High-mobility p-type semiconducting two-dimensional β-TeO_2. *Nat. Electron.* **4**, 277–283 (2021).
28. Jiang, K. et al. Mechanical cleavage of non-van der Waals structures towards two-dimensional crystals. *Nat. Synth.* **2**, 58–66 (2023).
29. Myronyuk, I. F., Mandzyuk, V. I., Sachko, V. M. & Gun'ko, V. M. Structural and morphological features of disperse alumina synthesized using aluminum nitrate nonahydrate. *Nanoscale Res. Lett.* **11**, 1–8 (2016).
30. Liu, K. et al. Puffing ultrathin oxides with nonlayered structures. *Sci. Adv.* **8**, eabn2030 (2022).
31. Quinn, G. D. *NIST Recommended Practice Guide: Fractography of Ceramics and Glasses*, 3rd edition, Special Publication (NIST SP) (National Institute of Standards and Technology, 2006).
32. Matsuo, H., mitsuhara, M., Ikeda, K., Hata, S. & Nakashima, H. Electron microscopy analysis for crack propagatin behavior of alumina. *Int. J. Fatigue* **32**, 592–598 (2010).
33. Studart, A. R., Gonzenbach, U. T., Tervoort, E. & Gauckler, L. J. Processing routes to macroporous ceramics: a review. *J. Am. Ceram. Soc.* **89**, 1771–1789 (2006).
34. Yang, X.-Y. et al. Hierarchically porous materials: synthesis strategies and structure design. *Chem. Soc. Rev.* **46**, 481–558 (2017).
35. Zallen, R. *The Physics of Amorphous Solids* (Wiley, 2008).
36. Frankberg, E. J. et al. Highly ductile amorphous oxide at room temperature and high strain rate. *Science* **366**, 864–869 (2019).
37. Hutchinson, J. W. & Suo, Z. Mixed mode cracking in layered materials. *Adv. Appl. Mech.* **29**, 63–191 (1991).
38. Navidtehrani, Y., Betegón, C. & Martínez-Pañeda, E. A unified abaqus implementation of the phase field fracture method using only a user material subroutine. *Materials* **14**, 1–19 (2021).
39. Böscke, T. S., Müller, J., Bräuhaus, D., Schröder, U. & Böttger, U. Ferroelectricity in hafnium oxide thin films. *Appl. Phys. Lett.* **99**, 102903 (2011).
40. Wei, Y. et al. A rhombohedral ferroelectric phase in epitaxially strained $Hf_{0.5}Zr_{0.5}O_2$ thin films. *Nat. Mater.* **17**, 1095–1100 (2018).
41. Cheema, S. S. et al. Enhanced ferroelectricity in ultrathin films grown directly on silicon. *Nature* **580**, 478–482 (2020).
42. Wang, J. et al. Transferred metal gate to 2D semiconductors for sub-1 V operation and near ideal subthreshold slope. *Sci. Adv.* **7**, eabf8744 (2021).
43. Zou, X. et al. Dielectric engineering of a boron nitride/hafnium oxide heterostructure for high-performance 2D field effect transistors. *Adv. Mater.* **28**, 2062–2069 (2016).
44. Zou, X. et al. Interface Engineering for high-performance top-gated MoS_2 field-effect transistors. *Adv. Mater.* **26**, 6255–6261 (2014).
45. Liu, Y. et al. Approaching the Schottky–Mott limit in van der Waals metal-semiconductor junctions. *Nature* **557**, 696–700 (2018).
46. Liu, H. & Peide, D. Y. MoS_2 dual-gate MOSFET with atomic-layer-deposited Al_2O_3 as top-gate dielectric. *IEEE Electron Device Lett.* **33**, 546–548 (2012).
47. Li, W. et al. Uniform and ultrathin high-*k* gate dielectrics for two-dimensional electronic devices. *Nat. Electron.* **2**, 563–571 (2019).
48. Favron, A. et al. Photooxidation and quantum confinement effects in exfoliated black phosphorus. *Nat. Mater.* **14**, 826–832 (2015).
49. Wang, G. et al. Introduction of interfacial charges to black phosphorus for a family of planar devices. *Nano Lett.* **16**, 6870–6878 (2016).
50. Shcherbakov, D. et al. Raman spectroscopy, photocatalytic degradation, and stabilization of atomically thin chromium tri-iodide. *Nano Lett.* **18**, 4214–4219 (2018).
51. Baeg, K.-J. et al. Organic non-volatile memory based on pentacene field-effect transistors using a polymeric gate electret. *Adv. Mater.* **18**, 3179–3183 (2006).
52. Marega, G. M. et al. Logic-in-memory based on an atomically thin semiconductor. *Nature* **587**, 72–77 (2020).
53. Tian, H. et al. Disorder-tuned conductivity in amorphous monolayer carbon. *Nature* **615**, 56–61 (2023).
54. Liu, L. When 2D materials encounter disorder. *Chin. Phys. Lett.* **40**, 56101 (2023).
55. Tian, H. et al. Unlocking more potentials in two-dimensional space: disorder engineering in two-dimensional amorphous carbon. *ACS Nano* **17**, 24468–24478 (2023).
56. Liu, S. et al. Degree of disorder-regulated ion transport through amorphous monolayer carbon. *RSC Adv.* **14**, 17032–17040 (2024).
57. Nagarajan, L. et al. A chemically driven insulator–metal transition in non-stoichiometric and amorphous gallium oxide. *Nat. Mater.* **7**, 391–398 (2008).
58. Sacépé, B. et al. Localization of preformed Cooper pairs in disordered superconductors. *Nat. Phys.* **7**, 239–244 (2011).

Acknowledgements

This work was supported by National Key R and D Program of China (2019YFA0307800, 2018YFA0305800, 2021YFA1400500 and 2020YFE0204200), Beijing Natural Science Foundation (JQ23004),

National Natural Science Foundation of China (12172005, 11890681, 11988102, 61888102, 52322311), Strategic Priority Research Program of Chinese Academy of Sciences under grant no. XDB33000000 and China Postdoctoral Science Foundation (BX20230002). L.W. is grateful for the support from the Youth Innovation Promotion Association of CAS (2020009). L. Liu acknowledges the supports of facilities from Peking Nanofab. We thank Materials Processing and Analysis Center, Peking University for assistance with XRD, XPS, SEM and EDS characterizations.

Author contributions

L. Liu conceived and supervised the project. R.L., Z.L., H.T., S.B. and Yanfeng Zhang carried out the sample preparations. R.L., Z.L., P.C.L., S.L., Y.W., L.Y.Z., US., G.Y., K.L., Y.H. and R.Z. performed the general characterizations. C.C. and X. Wei conducted the micro-CT characterization. T.W., X. Wang and J. Hong. performed the PFM measurements. L. Liao (Institute of Physics, Chinese Academy of Sciences), H.S., X.H., J.G., L.W., X.B. and P.G. performed the TEM measurements. Z.Y., K.W., Y.Y., L.B., L. Liao (Hunan University), J. He, H.-J.G. and Yue Zhang performed the device fabrication and measurements. X. Wei, J.M., E.W. and L. Liu developed the mechanism analysis. All authors discussed the results. R.L. and L. Liu wrote the manuscript with the inputs from all authors.

Competing interests

L.L. and R.L. hold a Chinese patent through Peking University (Chinese patent no. ZL 202210428539.1) on the technology related to the synthesis of large-sized lamella and thin flakes of AMOs and CMOs. The other authors declare no competing interests.

Additional information

Extended data is available for this paper at https://doi.org/10.1038/s44160-024-00657-8.

Supplementary information The online version contains supplementary material available at https://doi.org/10.1038/s44160-024-00657-8.

Correspondence and requests for materials should be addressed to Lei Liu.

Peer review information *Nature Synthesis* thanks Hyeon Suk Shin and the other, anonymous, reviewer(s) for their contribution to the peer review of this work. Primary Handling Editor: Alexandra Groves, in collaboration with the *Nature Synthesis* team.

[1]School of Materials Science and Engineering, Peking University, Beijing, China. [2]Key Laboratory of Interface Science and Engineering in Advanced Materials, Ministry of Education, Taiyuan University of Technology, Taiyuan, China. [3]Beijing National Laboratory for Condensed Matter Physics, Institute of Physics, Chinese Academy of Sciences, Beijing, China. [4]State Key Laboratory for Turbulence and Complex System, Department of Mechanics and Engineering Science, College of Engineering, Peking University, Beijing, China. [5]School of Aerospace Engineering, Beijing Institute of Technology, Beijing, China. [6]State Key Laboratory for Mesoscopic Physics and Frontiers Science Center for Nano-optoelectronics, School of Physics, Peking University, Beijing, China. [7]Peking University Nanchang Innovation Institute, Nanchang, China. [8]School of Physical Sciences, University of Chinese Academy of Sciences, Beijing, China. [9]Songshan Lake Materials Laboratory, Dongguan, Guangdong, China. [10]International Center for Quantum Materials, Collaborative Innovation Center of Quantum Matter, Peking University, Beijing, China. [11]Interdisciplinary Institute of Light-Element Quantum Materials and Research Center for Light-Element Advanced Materials, Peking University, Beijing, China. [12]State Key Laboratory for Mesoscopic Physics, Frontiers Science Centre for Nano-optoelectronics, School of Physics, Peking University, Beijing, China. [13]Key Laboratory for Micro/Nano Optoelectronic Devices of Ministry of Education and Hunan Provincial Key Laboratory of Low-Dimensional Structural Physics and Devices, School of Semiconductors (School of Integrated Circuits), Hunan University, Changsha, China. [14]Key Laboratory of Artificial Micro- and Nano-Structures of Ministry of Education, School of Physics and Technology, Wuhan University, Wuhan, China. [15]Academy for Advanced Interdisciplinary Science and Technology, Beijing Advanced Innovation Center for Materials Genome Engineering, Beijing Key Laboratory for Advanced Energy Materials and Technologies, School of Materials Science and Engineering, University of Science and Technology Beijing, Beijing, China. [16]School of Physics, Liaoning University, Shenyang, China. [17]These authors contributed equally: Ruijie Li, Zhixin Yao, Zhenjiang Li, Lei Liao, Huacong Sun, Chaonan Cong. ✉e-mail: l_liu@pku.edu.cn

https://doi.org/10.1038/s44160-024-00657-8

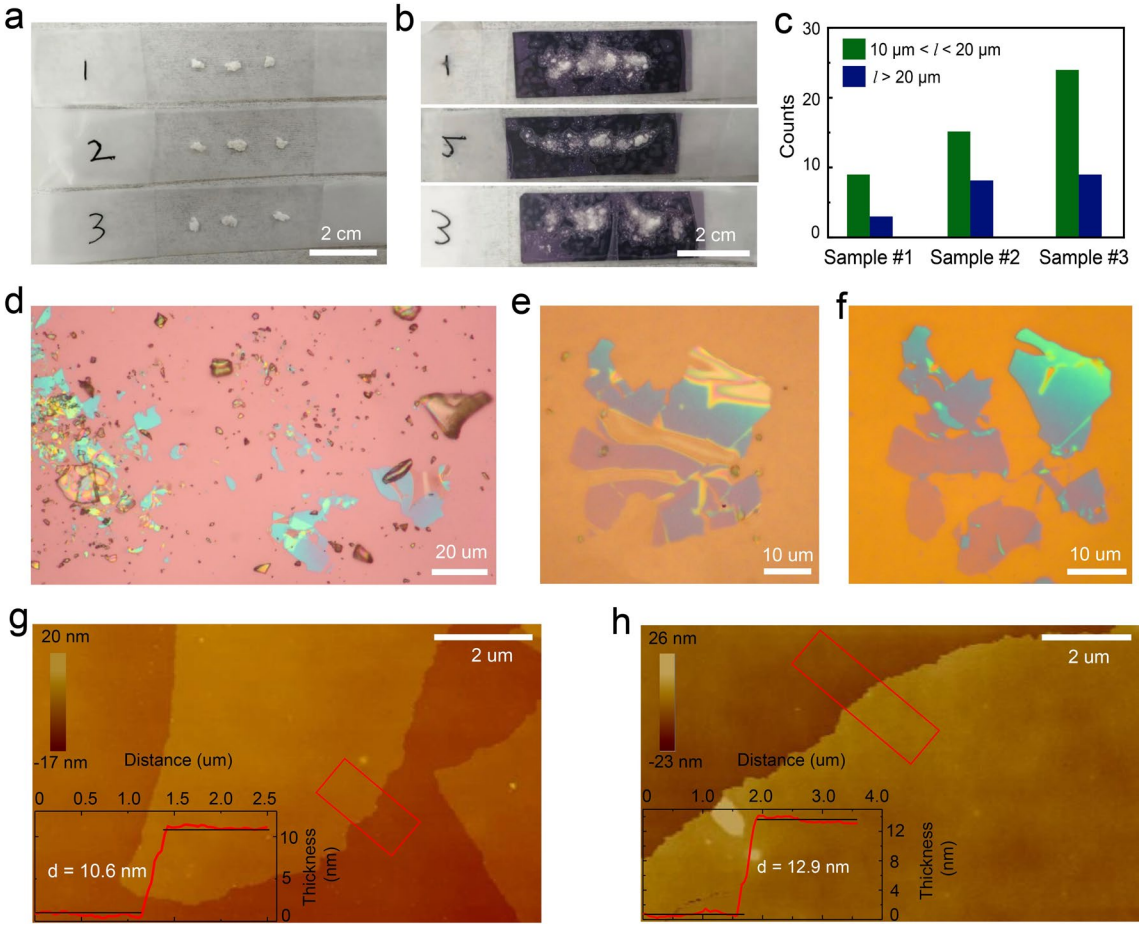

Extended Data Fig. 1 | Exfoliated AMOs thin flakes. a-b, Optical images of typical exfoliation of AMOs: putting foams on tapes (**a**) and pressing them on substrates (**b**). **c**, Statistics of the flakes' lateral size (l) on three substrates in (**b**). The numbers of ultrathin flakes (thickness d < 10 nm) found on three substrates are 1, 3, and 8, respectively. **d**, Low-mag optical image of exfoliated AMOs flakes, showing their high density and large dimensions. **e-f**, Optical images of ultrathin AMO flakes. **g-h**, AFM characterizations of two ultrathin flakes with thicknesses of 10.6 nm and 12.9 nm, respectively.

https://doi.org/10.1038/s44160-024-00657-8

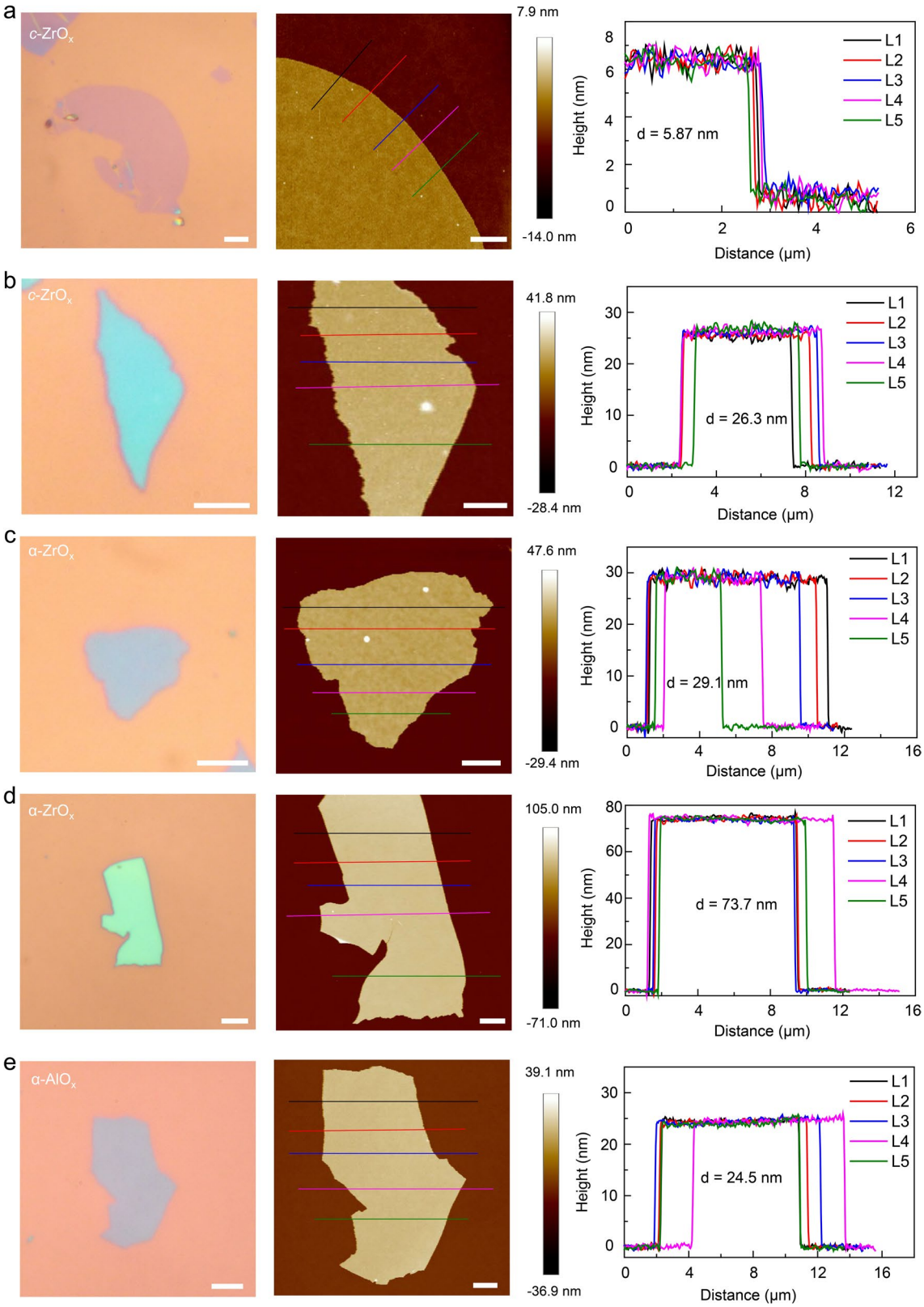

Extended Data Fig. 2 | Height uniformity of varied AMOs and CMOs flakes. a–e, Optical images (left column), AFM images with five lines highlighted (middle column), and height profiles (right column) corresponding to lines in AFM images. Scale bars: 5 μm (optical images, left column), 2 μm (AFM images, middle column).

https://doi.org/10.1038/s44160-024-00657-8

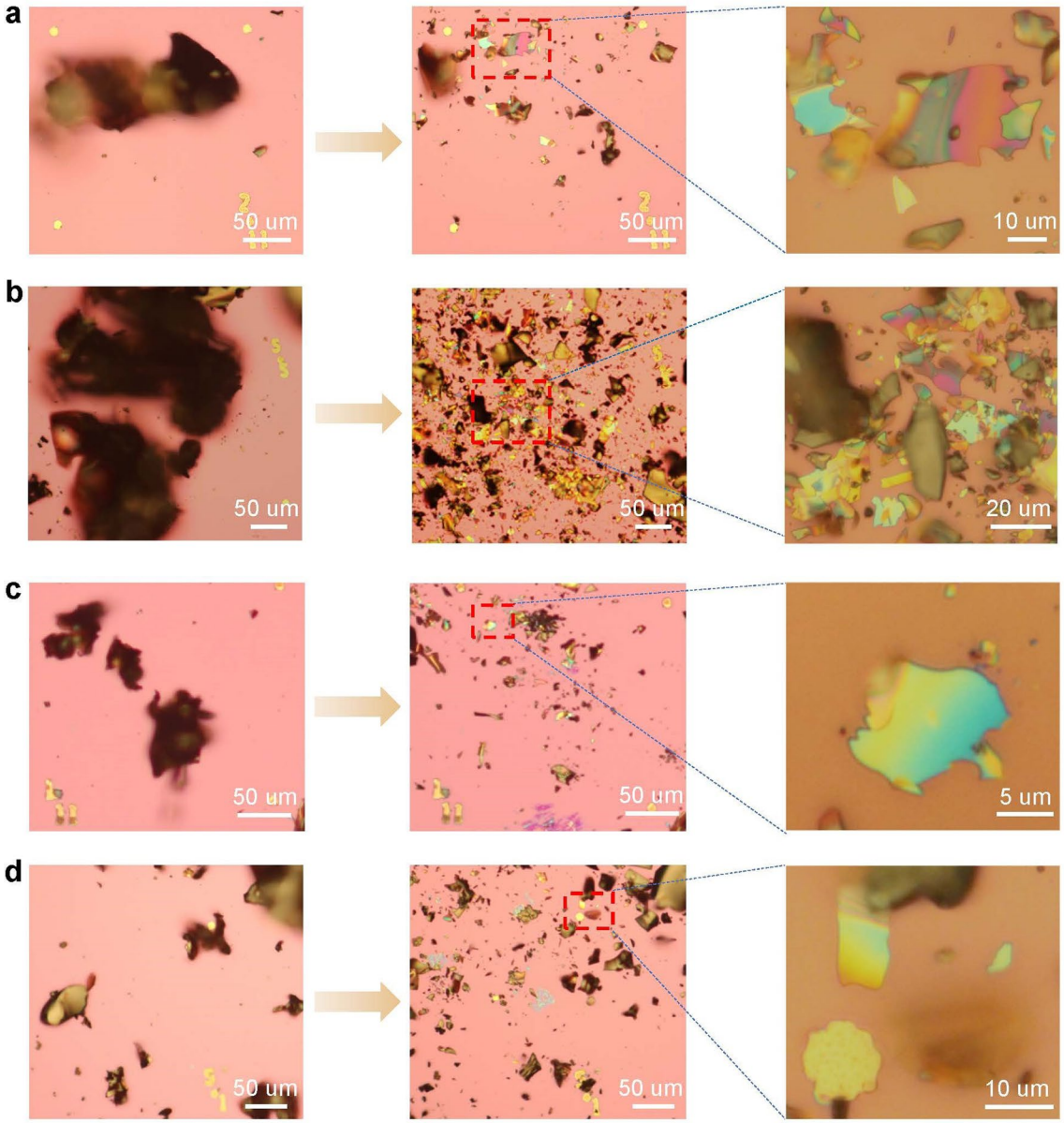

Extended Data Fig. 3 | Route #2 to fabricate AMOs flakes by directly crushing calcines on marked substrates. a–d, Optical images of four samples at different locations. From left to right panels: small pieces of α-AlO_x calcines on substrates (before crushing), low-magnification images after crushing with a tweeze tip, and zoomed-in images showing flakes with lateral sizes of ~10 μm. Samples from Route #2 were typically thicker than those from Route #1, that is, the tape exfoliation.

https://doi.org/10.1038/s44160-024-00657-8

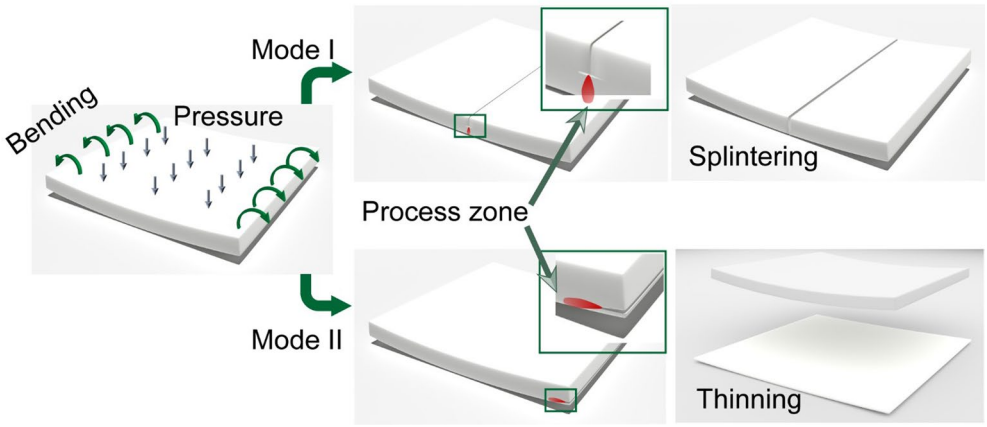

Extended Data Fig. 4 | Schematics of the exfoliation mechanism from lamellae to thin flakes. Note that lamellae are not entirely flat but slightly curved (Supplementary Fig. 1b, c). Pressing the curved flake on the rigid substrate introduces bending on the material and thus causes two possible fracture modes. In Mode I, the flake cleaves along the cross-section into two pieces of equal thickness, introducing shrinkage of the lateral size. In Mode II, the crack propagates along the longitudinal section so that a thinner flake exfoliates from the original piece.

https://doi.org/10.1038/s44160-024-00657-8

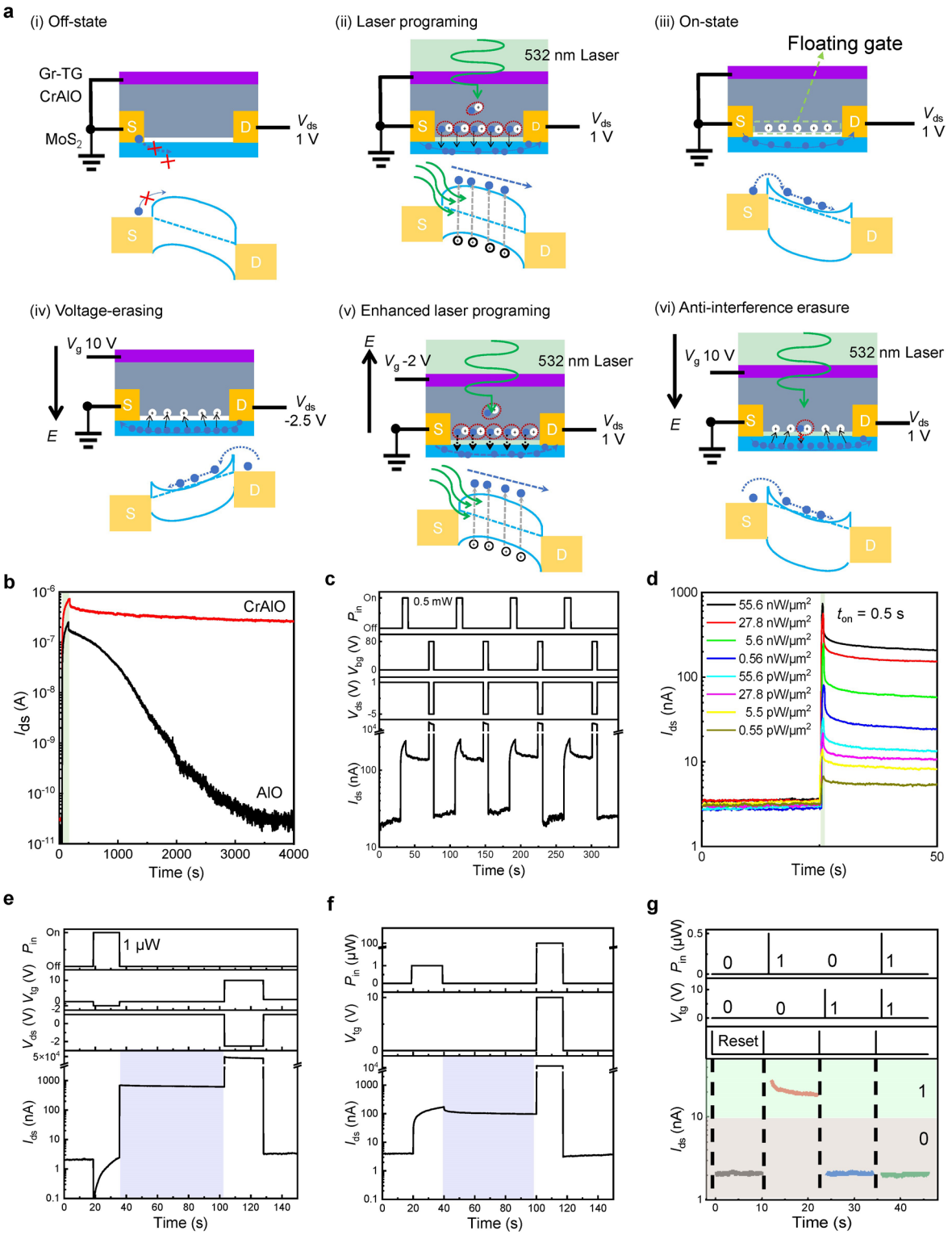

Extended Data Fig. 5 | See next page for caption.

https://doi.org/10.1038/s44160-024-00657-8

Extended Data Fig. 5 | Photon-programming floating gate devices. **a**, Schematics of the devices' operations and band diagrams(Purple box: Gr-TE, Grey box: CrAlO, Blue box: MoS_2, Blue balls: electron, White balls: hole). The operation is based on the considerable adsorption of green light in the CrAlO layer and electron tunneling through the nanogap between monolayer MoS_2 and CrAlO. Without the gating or illumination, the channel is in the low current (OFF) state (Step i). With the illumination of a 532 nm laser, photon-generated electron-hole pairs occur in CrAlO, followed by the pair dissociations and the electron transfer from CrAlO to MoS_2 (Step ii). When turning the light off, due to the nanogap, holes nearby the interface cannot be combined and thus can exist, serving as a photon-programming floating gate to turn on the device (Step iii). The near-interfacial holes can be erased with the assistance of gate voltages. For example, with a 10 V of the top-gate voltage, the injection of an electron from MoS2 back to CrAlO takes place, eliminating the floating gate (Step iv). The laser programming step can be enhanced by applying a negative gate voltage (V_{tg} = -2 V) which promotes more efficient electron tunnelling and higher hole density left in CrAlO for floating gating (Step v). The positive top-gate voltage also restricts only one-way electron tunnelling (from MoS_2 to CrAlO) even under illumination, giving rise to a robust voltage erasure (Step vi). **b**, Comparison of CrAlO and AlO as top-gate dielectrics. With the same device configurations and laser stimulus, a non-volatile optoelectronic response is revealed for the CrAlO-gated device manifested by the retained channel current without suppression for at least 4000 s, in sharp contrast to an unstable current with fast decay in an AlO-gated device. **c**. Voltage erasing process by the back-gate voltage. By applying 80 V of the back-gate voltage, the device is turned on with an enhanced electron density, and a slightly negative bias (-5 V) is also helpful for the electron tunnelling (from MoS_2 back to CrAlO) to erase the floating gate. After the voltage erases, the channel current drops back to the off-state level. **d**, Different current states programmed by the intensity of light. **e**-**f**, Operations corresponding to Steps v and vi in a. Enhanced laser programming is achieved by applying a −2 V of top-gate voltage which leads to a ten-times larger retained current (1000 nA in e versus 100 nA in f). During the top-gate voltage erasing process, the concurrent illumination (even at higher power) does not affect the elimination of the floating gate stored in the previous run of illumination (**f**). **g**, One in-sensor logic operation, the negation of an implication ($\neg(p \rightarrow q)$) where p is the laser illumination and q is the top-gate voltage.